Journal of Applied Physics

Tailoring impact debris dispersion using intact or fragmented thermite projectiles

Cite as: J. Appl. Phys. **128**, 155108 (2020); https://doi.org/10.1063/5.0023990
Submitted: 03 August 2020 . Accepted: 09 October 2020 . Published Online: 21 October 2020

K. Ryan Bratton, Kevin J. Hill, Connor Woodruff, Colton Cagle, Michelle L. Pantoya, Joseph Abraham, Liang Wei, and Pascal Dube

View Online
Export Citation
CrossMark

ARTICLES YOU MAY BE INTERESTED IN

Optical absorption window in Na_3Bi based three-dimensional Dirac electronic system
Journal of Applied Physics **128**, 155707 (2020); https://doi.org/10.1063/5.0022669

Velocity and mass density of the ejecta produced from sinusoidal grooves in laser shock-loaded tin
Journal of Applied Physics **128**, 155903 (2020); https://doi.org/10.1063/5.0022940

Dislocations in chemical vapor deposition diamond layer detected by confocal Raman imaging
Journal of Applied Physics **128**, 155302 (2020); https://doi.org/10.1063/5.0021076

AIP Publishing

© 2020 Author(s).

Journal of Applied Physics ARTICLE scitation.org/journal/jap

Tailoring impact debris dispersion using intact or fragmented thermite projectiles

Cite as: J. Appl. Phys. **128**, 155108 (2020); doi: 10.1063/5.0023990
Submitted: 3 August 2020 · Accepted: 9 October 2020 ·
Published Online: 21 October 2020

View Online Export Citation CrossMark

K. Ryan Bratton,[1] Kevin J. Hill,[1] Connor Woodruff,[1] Colton Cagle,[1] Michelle L. Pantoya,[1,a)] Joseph Abraham,[2] Liang Wei,[2] and Pascal Dube[3]

AFFILIATIONS

[1]Mechanical Engineering Department, Texas Tech University, Lubbock, Texas 79409, USA
[2]Karagozian & Case Inc., Glendale, California 91203, USA
[3]Matsys Inc., Sterling, Virginia 20164, USA

[a)]**Author to whom correspondence should be addressed:** Michelle.pantoya@ttu.edu. **Telephone:** 806 834 3733

ABSTRACT

A high-velocity impact-ignition testing system was used to study the dynamic response of brittle thermite projectiles impacting an inert steel target at velocities of 850 and 1200 m/s. The projectiles included consolidated aluminum and bismuth trioxide that were launched by a propellant driven gun into a catch chamber equipped with high-speed imaging diagnostics. The projectiles passed through a break-screen at the entrance to the chamber and either fragmented upon penetrating the break-screen or remained intact prior to impacting the steel target. In all cases, the projectiles pulverized upon impact, and a reacting debris cloud spreads through the catch chamber. At lower impact velocities, the fragmented and intact projectiles produced similar flame spreading rates of 217–255 m/s. At higher impact velocities, the intact projectile produced the slowest average flame spreading rate of 179 m/s because debris rebounding was limited by the length of the projectile and the resulting debris field was highly consolidated in the radial direction. In contrast, the fragmented projectile rebounded into a well dispersed debris cloud with the highest, 353 m/s, flame spreading rate. A kinetic energy flux threshold was proposed as a means for describing the shift in observed debris dispersion and flame spreading rates. A reactivity model was developed based on particle burn times using a computational fluid dynamics code that incorporated heat transfer and particle combustion in a multiphase environment to understand how the particle size influenced flame spreading. Results from the model show a trade-off between faster reactivity and increased drag inhibiting movement for smaller particle debris.

Published under license by AIP Publishing. https://doi.org/10.1063/5.0023990

INTRODUCTION

Thermites are defined here as a mixture of metal fuel combined with metal oxide powders and can be used as structural reactive materials (SRMs).[1] As an SRM, the powder mixture is pressed into a highly consolidated form that is generally inert under ambient conditions but can ignite and chemically react under high strain rate loading (i.e., 10^4–$10^5\,s^{-1}$) conditions, as in high-velocity impact. Typically, the SRM contains a binder (such as polytetrafluoroethylene, PTFE) that aids in consolidating the powder mixture and provides structural integrity.[2] Without a binder, a consolidated thermite is naturally more brittle and will more easily fragment.[3]

Recently, impact behavior of brittle materials has received much attention due to the practicality of understanding composite fracture and failure. Hooper[3] performed a series of high-velocity experiments on consolidated aluminum powder projectiles that penetrated thin plates. The ensuing debris was captured using a clever soft-catch method involving a lot of shaving cream downstream from the penetrated plate. The projectiles experienced negligible reaction and were analyzed for their size distribution as a function of impact velocity. Generally, the majority of the debris maintained a size distribution less than 1 mm but shifted from an exponential to a power-law distribution for impact velocities ranging from 600 to 1200 m/s, respectively.

Ames[4] developed a vented chamber apparatus for interpreting impact data and his approach has been used as a benchmark for many impact-ignition studies. Ames[2] studied several metal fuel powders (including Al) with several binder concentrations (including PTFE) that were consolidated into projectiles and launched into a catch chamber. The experimental design purposefully used a

Published under license by AIP Publishing.

target skin at the entrance to the chamber to semi-seal the chamber and enable a calorific measurement of energy deposition. The target skin was a 1/16 in. thick mild steel plate that was perforated by the projectile. Due to relatively low strength of all projectiles, the initially consolidated projectile fragmented into a debris field of particles inside the chamber after penetrating the target skin.

Zhang *et al.*[5] also performed high-velocity impact testing on projectiles composed of Al and PTFE as well as an intermetallic formulation of tungsten (W) and zirconium (Zr). Their energy analysis was supplemented with a model that coupled evaluation of shock temperature controlled by the input stress that was directly a function of the impact velocity with kinetic models to account for the extent of chemical reaction under shock loading. Their model provided a direct method for comparing the measured pressure response with the phenomenological conditions of the models and both were in good agreement. Their model inspired our consideration of the thermal, reactive, and fluid dynamics of debris downstream of the impact event.

Both Ames[4] and Zhang *et al.*[5] quantify variations in dynamic pressure throughout the impact event by capitalizing on a semi-sealed chamber. The experiments designed here do not include pressure measurements but instead focus on the visual data associated with fragmentation and flame spreading. Future work will augment the chamber with pressure transducers to further characterize projectile reactivity. The objective of this study was to characterize the high-velocity impact and reaction behavior using high-speed imaging data of brittle thermite projectiles that are either intact or fragmented upon impacting a target. This study extends previous work because (1) the formulation is without the binder and purely a thermite that includes $Al + Bi_2O_3$ and is, therefore, brittle and (2) reactivity resulting from the impact is analyzed in terms of the debris field and flame spreading behavior through the chamber as a function of fragmented compared with intact projectiles for low (850 m/s) and high (1200 m/s) impact velocity cases. Previous work examined projectiles that were intermetallic or metal fuel and binder with limited investigation on brittle thermite projectiles. Brittle projectiles are particularly interesting because they pulverize into a dust-like debris field upon impact without significant energy absorption by the target. Because the target does not deform with impact, energy is mainly rebounded such that the dynamics of particle dispersion affects flame spreading. Also, previous work examined either fragmented[2] or intact[5] projectiles but a comparison between reactive behaviors of these two cases is a useful contribution toward understanding a material's response to high strain rate loading conditions (i.e., 10^4–$10^5\,s^{-1}$). Experimental measurements are further supplemented in terms of a fluid based thermal–chemical reaction model developed to resolve particle combustion and fluid dynamic processes following the impact. Results from the model are compared to experimental observations, and mechanisms describing flame spreading behavior are discussed.

EXPERIMENTAL

The projectiles used in this study were manufactured by MATSYS Inc. (Sterling, Virginia) and include Al and Bi_2O_3 powders that were isostatically pressed to 98% theoretical maximum density in the shape of cylinders with 0.95 cm diameter and length. This cylindrical volume required 1.95 g of powder and the mixture composition, density, and porosity remained constant for all projectiles examined. The cylinder was encased in a 0.410 shot gun shell, loaded into a powder gun, and fired into a catch chamber. Two impact velocity regimes were selected for investigation: 850 and 1200 m/s. The shot gun shell, powder gun, and catch chamber assembly (called the High-velocity Impact-ignition Testing System, HITS) and additional experimental details can be found in Hill *et al.*[6] but are described briefly below.

The catch chamber is a $45.7 \times 14 \times 14\,cm^3$ (L × W × H) rectangular chamber with a custom-built break-screen fixed onto the open face of the chamber [see Fig. 1(a)]. The projectile passes

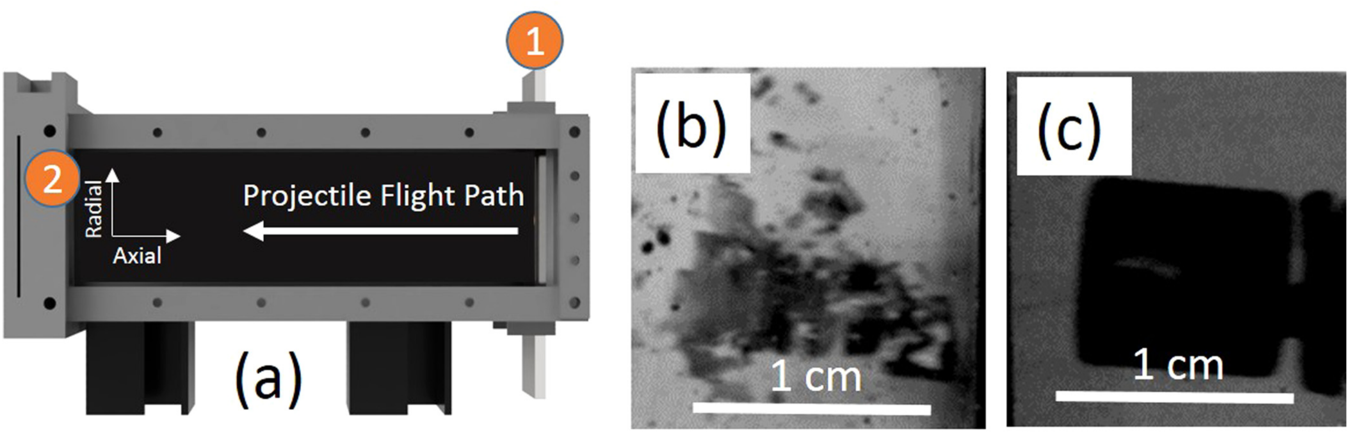

FIG. 1. (a) Catch chamber schematic used to collect visual data resulting from projectile impact. The chamber includes a (1) penetration break-screen through which the projectile enters the chamber and (2) a steel target plate. Positioned perpendicular to the window and not pictured here is a high-speed camera. Photographs of a (b) fragmented and (c) intact projectile in flight through the catch chamber after passing the break-screen are also included.

Published under license by AIP Publishing.

through a break-screen composed of a thin paper with thin pieces of aluminum foil biased with a 9 V battery to trigger the high-speed camera data acquisition system. The high-speed camera enabled measurements of impact velocity, projectile flight and impact, and flame spreading throughout the chamber after the impact. In Fig. 1(a), the target was a polished 4130 steel plate 0.95 cm thick and clamped into place by mounts on the upper and lower faces of the catch chamber. Behind the target plate was a 2.54 cm thick plate to prevent the projectile from escaping the catch chamber in the unlikely event of total target plate penetration (for safety). After impact, the debris was very fine particles (micrometer to millimeter scale), and quantitative analysis of debris size from the video data was not possible. At least 25 tests were performed for each impact velocity and at least five fragmented projectiles and five intact projectiles were analyzed for each impact velocity. It is noted that projectile launch generally resulted in very flush impacts but projectiles that may have tilted also fragmented upon penetration of the break-screen and enabled analysis of fragmented projectiles that were compared with the intact projectiles impacting the target. Figures 1(b) and 1(c) illustrate a fragmented and an intact projectile.

Visual data from the impact and reaction event were captured by a Phantom v710 (Wayne, NJ) color camera with a 20 mm wide angle Nikon lens at an f-stop of 1/16. This camera's field of view captured the long (axial)-axis of the catch chamber for far-field (i.e., $13.5 \times 6.75\ \text{cm}^2$) visualization of penetration through the break-screen throughout projectile flight to the impacting target. The spatial resolution of 512×512 pixels was set to record video at 46 kHz with an exposure time of 3 μs. Various flash bulbs were also used to improve lighting conditions and imaging the highly dynamic event. This macroscopic view captured projectile impact, pellet pulverization, debris cloud formation, and flame spreading through the chamber. The spreading rate of the flame was determined from high-speed video analysis of the leading edge of the flame front using frame-by-frame tracking software from the Phantom Camera Controller (PCC 3.0). It is noted that the flame continues to illuminate the chamber beyond the camera's recording such that the flame duration is beyond 3 ms but an exact burn time could not be determined.

MODEL

A particle combustion and heat transfer model was developed and implemented into a computational fluid dynamics code to further understand the experimental observations of flame spreading behavior. The model assumes particle reactivity at conditions after the impact event to model the extent of reaction as a function of time for varied particle sizes. In this case, aluminum oxidation was considered for two separate reactions: (1) a thermite consisting of $Al + Bi_2O_3$ and (2) Al particles burning with surrounding gas phase oxygen from the ambient air environment identified as $Al + O_2$. For the thermite, both reactants are considered as one element of a spherical particle that has properties of Al and Bi_2O_3. For Al oxidizing in air, the model assumes properties of Al. In both cases, the burn times are calculated according to the D^2 law which is valid for burning particles assumed larger than 10 μm diameter.[7]

Figure 2 illustrates schematically the model domain that is confined to a geometry similar to the catch chamber in Fig. 1. A

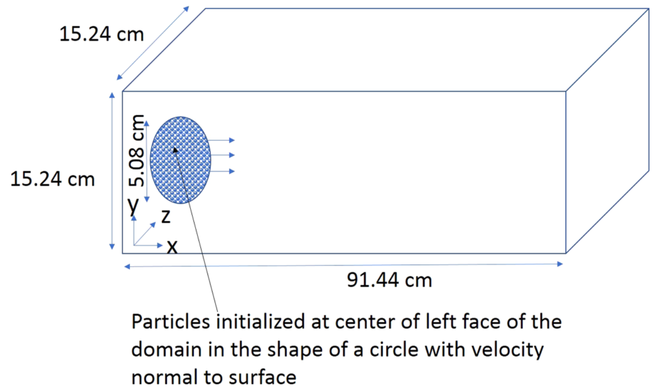

FIG. 2. Schematic illustrating particle combustion and heat transfer model used to simulate flame spreading behavior as a function of particle debris size.

debris cloud of particles with prescribed average diameter are centralized at the center of the left face and spread to the right where their velocity can be adjusted but for this analysis, the particle velocity was set to 100 and also 400 m/s to coincide with the minimum and maximum flame spreading rates observed experimentally.

The mass burn rate and heat of combustion provide the energy generated by the particle, E_{in}. Energy transfer is modeled at the particle surface described by Altman[8] and Allen *et al.*,[9] shown in Eq. (1), where E_{in} is the heat generated by combustion, E_{sur} is the conductive heat transferred to the surroundings given in Eq. (2), E_{rad} is the radiation to the surroundings and assumed negligible, and E_{par} is the heat transferred to the particle from the high temperature environment as shown in Eq. (3),

$$E_{in} = E_{sur} + E_{rad} + E_{par}, \tag{1}$$

$$E_{sur} = k(T_s - T_a)A, \tag{2}$$

$$E_{par} = mc_p\Delta T. \tag{3}$$

Note that T_s is the steady state temperature assumed to be the ignition temperature, T_a is the surrounding temperature assumed to be the flame temperature for the $Al + Bi_2O_3$ reaction, ΔT is the temperature difference between T_s and T_a, m and c_p are the mass and specific heat of the particle, and k is the thermal conductivity defined using Eq. (4),[8]

$$k = \frac{k_f \dfrac{Nu \cdot \lambda}{D}}{k_f + \dfrac{Nu \cdot \lambda}{D}}. \tag{4}$$

In Eq. (4), λ is the thermal conductivity of the gas, Nu is the Nusselt number, and k_f is the free-molecular conductive heat

Published under license by AIP Publishing.

transfer coefficient expressed as Eq. (5),[8]

$$k_f = \frac{\alpha_E P C_g}{8T_a} \cdot \frac{\gamma + 1}{\gamma - 1}. \tag{5}$$

In Eq. (5), α_E is the energy accommodation coefficient which can be adjusted to fit the experimental data and has a maximum value of 0.005.[8] For Nu, Whitaker's correlation for spheres was used as an approximation for forced convection representing the relatively high flame spreading rates observed.[10] Also, P is the ambient pressure, c_g is the average gas molecular velocity, and γ is the ratio of specific heats. For aluminum combustion with oxygen, the average gas molecular velocity is computed as Eq. (6)[9] with k_b representing the Boltzmann constant and m_{o_2} is the mass of a gas molecule,

$$c_g = \left(\frac{8k_b T_a}{\pi \cdot m_{o_2}}\right)^{1/2}. \tag{6}$$

The Lagrangian tracer particles are modeled by solving the Lagrangian equations of motion which are simply the kinematic equations for particles shown in Eqs. (7) and (8),[11]

$$D_t x = v, \tag{7}$$

$$D_t v = a. \tag{8}$$

The force acceleration vector due to drag is calculated using a classical drag force law in Eq. (9),[11]

$$a_D = -\frac{f_D}{m} = -\frac{0.5 C_D \rho |v_d|^2 A}{m} \frac{v_d}{|v_d|} = -C_D \frac{3|v_d|^2}{8r} \frac{v_d}{|v_d|}. \tag{9}$$

In Eq. (9), C_D is the drag coefficient (≈0.5 for a sphere), r is the particle radius, and here v_d is the particle drift velocity, defined in Eq. (10),

$$v_d \equiv v_{particle} - v_{fluid}. \tag{10}$$

RESULTS AND DISCUSSION

Table I summarizes the flame spreading rate in the axial direction as a function of impact velocity and projectile integrity along with the standard deviation in measurements. The standard deviation is based on variations measured between five experiments for each case. In all cases, the target remained intact and did not deform by the impact events.

Table I shows fragmented projectiles produce higher flame spreading rates than intact projectiles regardless of impact velocity. But the difference in the average flame spreading rate was only 38 m/s for an impact velocity of 850 m/s, and the difference increased to 174 m/s for an impact velocity of 1200 m/s, i.e., an order of magnitude larger difference between the fragmented and intact cases. Another interesting observation was the reversed trends associated with projectile integrity and increasing impact velocity. Specifically, the intact pellet exhibited a 19% *decrease* in the flame spreading rate when the impact velocity increased from 850 to 1200 m/s, while the fragmented pellet exhibited 32% *increase* over the same increase in impact velocities.

TABLE I. Table of flame spreading rate for both impact velocities and projectile integrities. Uncertainty were generated using one standard deviation of tests.

Velocity (m/s)	Projectile integrity	Flame spreading rate (m/s)	Kinetic energy flux (MJ/m^2)
850	Intact	217 ± 21	9.94×10^3
850	Fragmented	255 ± 30	9.94×10^1
1200	Intact	179 ± 11	1.98×10^4
1200	Fragmented	353 ± 67	1.98×10^2

Figure 3 illustrates the flame spreading behavior summarized in Table I. It is noted that the lighting appears different for each case and the apparent differences are an artifact of the position and type of flashbulb used to optimize visualization. In Fig. 3, time 0.0 corresponds to the first frame of impact and subsequent frames illustrate flame spreading upon impact at the indicated time interval. A noticeable difference in flame spreading behavior was observed for the intact projectile at 1200 m/s impact velocity. At this higher impact velocity, directed energy of the intact projectile appears to produce flame spreading more dominantly in the radial direction and a relatively non-dispersed debris cloud with a planar reaction front propagating in the axial direction. The length of the intact projectile may inhibit rebounding motion in the axial direction and restrict the debris cloud dispersion and reactivity to the radial direction. When the projectile is fragmented prior to impact, there is approximately a ten-time increase in the impacting area observed from the experimental still-frame images at times prior to impact (e.g., prior to time 0.0). The resulting particle debris rebounds in a well dispersed cloud with an axial spreading rate on the order of 353 m/s, the highest spreading rate observed. But, at the lower impact velocity, both intact and fragmented projectiles demonstrate similar flame spreading behavior (Fig. 3) with well dispersed debris clouds rebounding in the axial direction at similar flame spreading rates on the order of 217–255 m/s. It is noted that for the 850 m/s impact velocity, the fragmented projectile was locally fragmented at the front surface of the projectile such that a larger fragment appears in the first frame in Fig. 3 and is not to be mistaken for an intact projectile.

In an attempt to quantify the distinctions in visual data between high vs low impact velocity and fragmented vs intact projectile behavior described above, we propose a parameter called the kinetic energy flux (KE'') that includes the influence of impact velocity and area associated with the intact or fragmented projectile impacting the target for a given projectile mass. Table I includes calculations for KE'' associated with impacting particles calculated using Eq. (11),

$$KE'' = 1/2\,\mathrm{mV}^2/\mathrm{A}\,. \tag{11}$$

In Eq. (1), m is the projectile mass and assumed constant for all projectiles (1.95 g), V is the impact velocity (850 or 1200 m/s), and A is the area of impact on the target estimated to be a circular

Published under license by AIP Publishing.

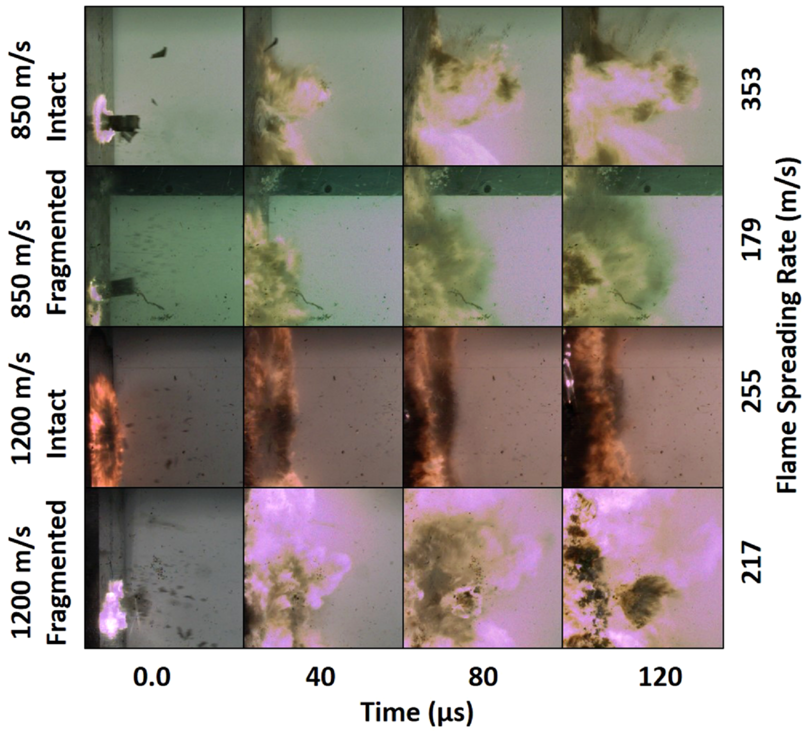

FIG. 3. Sequence of still-frame, time-stamped images showing the differences in flame spread due to projectile integrity and impact velocity. The average flame spreading rate is also included from data in Table I. Color variations in images are due to arrangement of flashbulbs used to optimize visualization.

area of diameter equivalent to the projectile diameter (i.e., 0.95 cm) for the intact projectile (i.e., $1 \times 10^{-4}\,m^2$, see Fig. 1). Still-frame images of fragmented projectiles upon impact (see Fig. 1) show a good estimate of the impact diameter is about 10 cm or ten-times the projectile diameter with an area of $7.1 \times 10^{-3}\,m^2$. Table I shows there is an order of magnitude higher kinetic energy flux associated with the 1200 m/s impact velocity and intact projectile that may be a threshold impact energy flux that alters the dynamics of rebounding fragments. Values below a kinetic energy flux on the order of $1 \times 10^4\,MJ/m^2$ result in well dispersed fine particle debris clouds with a stochastic reaction front propagating in the axial and radial directions. Values higher than this kinetic energy flux threshold result in a shift toward radial debris dispersion with a more consolidated debris field having a more planar flame front. A more consolidated and less well disbursed debris field will limit oxygen availability for fuel burning such that the dust cloud combustion stoichiometry may be less than optimum to promote complete combustion. More investigation of the kinetic energy flux is needed to truly establish a relationship between parameters effecting debris dispersion and rebound behavior but Fig. 3 suggests energy coupling between impact velocity, debris dispersion, and flame spreading.

A chemical reaction model that includes heat transfer and fluid dynamics was developed to understand the flow and reaction characteristics of a debris field composed of small or large particles. The input material reaction parameters for the application of the model are shown in Table II. The model assumes that the reaction results from rapid mixing of particles behind the shock front induced upon impact due to plastic deformation, jetting, fracture, and pore collapse such that the temperature in the reaction zone is assumed to be the adiabatic flame temperature for the $Al + Bi_2O_3$ or $Al + O_2$ reaction, respectively. The assumption is that the kinetic energy of the impact event transfers to the fracture (mechanical) energy in the impacted material elevating temperature in the multiphase medium initiating reactions that continue from the chemical energy released upon combustion. While the particle size distribution within the debris cloud could not be evaluated from the video data, Hooper[3] studied the size distribution of brittle reactive materials that fractured upon penetration of a thin plate at impact velocities similar to those examined here. He showed that the majority of particles are less than 1 mm in size and peak between 50 and 500 μm. In this analysis, particle size was assumed constant and two cases were studied: 0.05 mm and 0.1 mm average diameter particles. The ignition temperature for the $Al + Bi_2O_3$ reaction is estimated at 870 K from Piekiel *et al.*[12] and the ignition temperature for Al oxidation with air is estimated to be 973 K from Werley *et al.*[13] Ignition temperature is a function of particle size such that these estimates are based on the literature for fine powder size dispersions, consistent with the fine particle debris fields observed here.

Figure 4 shows results from the model and illustrates the influence of variation in particle size on the extent of reaction, the variation in the type of reaction (i.e., see Table II for complete reactions labeled here as: $Al + O_2$ or $Al + Bi_2O_3$), and the influence of the particle velocity. Figure 4(a) represents particles moving at 100 m/s, while Fig. 4(b) represents particles moving at 400 m/s. The flame

Published under license by AIP Publishing.

TABLE II. Reaction parameters for the Al + Bi_2O_3 and Al + O_2 particle burning analysis of extent of reaction.

Reaction	Density (g/cm^3)	Heat of combustion (kJ/cm^3)	Particle velocity (m/s)	Ignition temperature (K)	Flame temperature (K)	Total mass (g)
$2Al + Bi_2O_3 \rightarrow Al_2O_3 + 2Bi$	7.188	15.22	400	870	3250	1.0
$4Al + 3O_2 \rightarrow 2Al_2O_3$	2.7	83.85	400	973	3535	1.0
$2Al + Bi_2O_3 \rightarrow Al_2O_3 + 2Bi$	7.188	15.22	100	870	3250	1.0
$4Al + 3O_2 \rightarrow 2Al_2O_3$	2.7	83.85	100	973	3535	1.0

spreading rates were selected to represent upper and lower limits of the measured values. The most interesting observation from comparing Figs. 4(a) and 4(b) is that the extent of burned products increases considerably for aluminum reacting with surrounding oxygen gas as the particle speed increases, whereas the particle speed has a negligible effect on the extent of burned products from the thermite reaction. Higher particle velocities allow more oxygen availability to the fuel particles and facilitate their burning. Comparing Figs. 4(a) and 4(b) also suggests that while the solid oxidizer (i.e., Bi_2O_3) may promote reactivity, oxygen from the environment may enable secondary reactions and produce flame spreading for a longer duration compared to the thermite alone. Experimental work confirming the model prediction would require modifications to the reaction chamber that would control the environment to provide an argon (inert) vs oxygen gas environment comparison; this work is currently on-going. Figure 4 also shows that smaller particle debris burn at a faster rate than larger particle debris, as expected from the D^2 law for particle burning.[7]

Figure 5 shows a series of still-frame images that illustrate the extent of burned product residue as a function of time for the two particle sizes, two oxidation reactions, and two particle velocities analyzed. Consistent with Fig. 4, smaller particles produce greater concentrations of product species visually apparent by the increased dispersion of red particles in all images of Fig. 5. It is interesting to note that the flame front appears more condensed and planar for the thermite particles with a slower velocity (100 m/s) but at higher velocity, thermite particles disperse in the axial and radial directions. Experimentally, the slowest flame spreading rate is also associated with a highly consolidated debris field and planar reaction front. For the thermite at higher velocity and at later times, the flame front becomes more stochastic as the cloud of particles disperses in the domain, consistent with the high flame spreading behavior of the fragmented projectile at 1200 m/s impact velocity. The opposite is true for the aluminum particles reacting with gaseous oxygen from the environment: higher particle velocities produce a more condensed, planar product species field. The thermite oxidizer (Bi_2O_3) may inherently be more dispersed through the particle debris field allowing better dispersion of thermite product species compared with aluminum oxidation in the oxygen environment. Generally, for both oxidation reactions, smaller particles exhibit slower progression in the axial direction when compared with larger particles. The sequence of still-frame images from the model shown in Fig. 5 visualizes the behavior of burned products that are quantified in Fig. 4. Generally, the

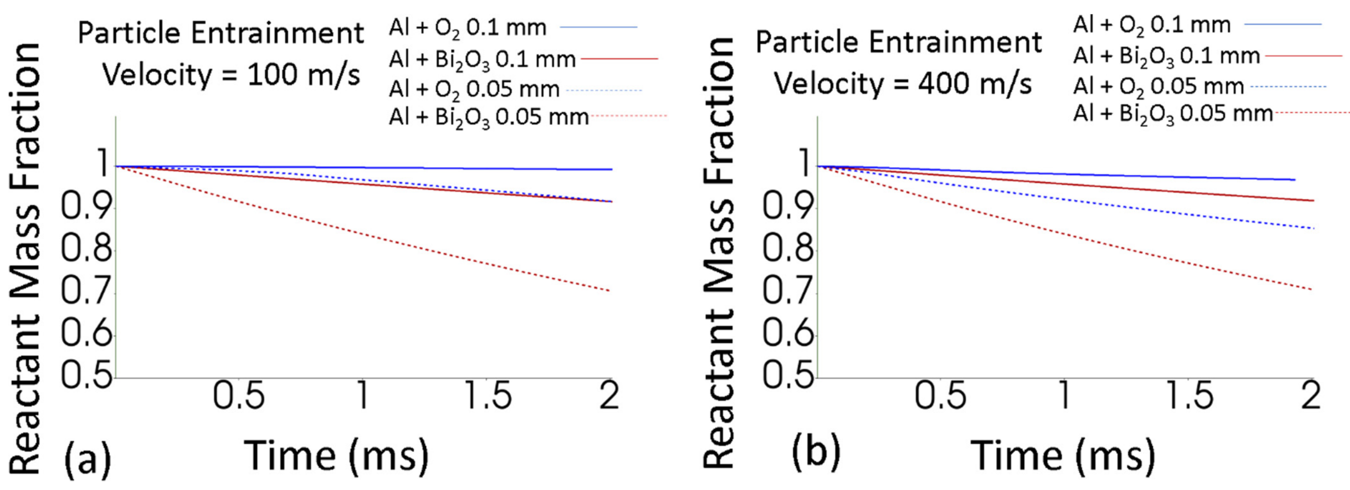

FIG. 4. Comparison between unburned mass fraction as a function of time for two average diameter particles and two representative aluminum oxidation reactions indicated in the legend above both graphics. (a) Particles are moving at 100 m/s and (b) particles are moving at 400 m/s. Note red curves are for Al + Bi_2O_3 with solid line representing 0.1 mm diameter particles and dashed lines representing 0.05 mm diameter particles, and blue curves are similarly formatted for Al + O_2 reactions.

Published under license by AIP Publishing.

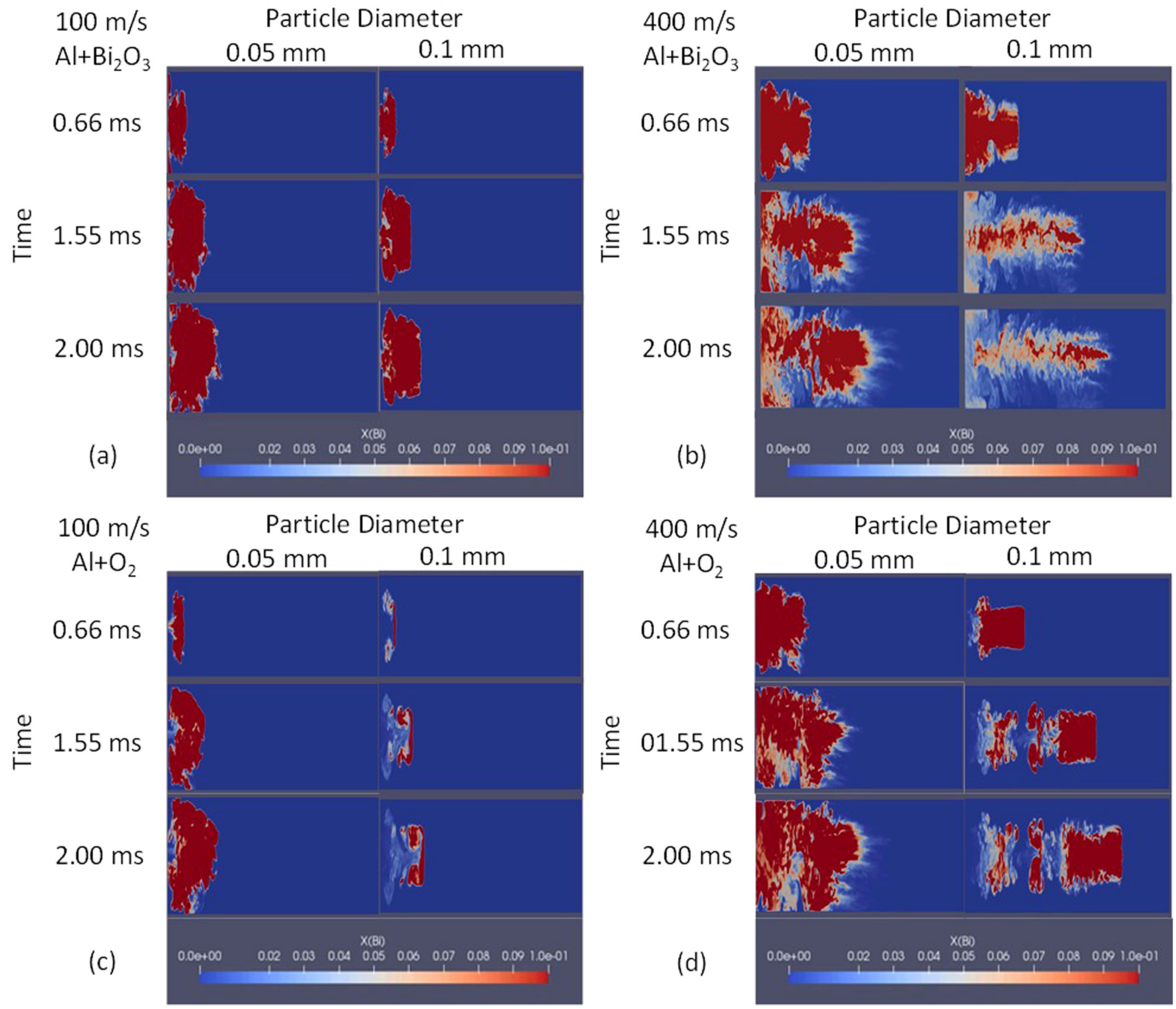

FIG. 5. Mass fraction of product species for three times, two different oxidation reactions indicated as Al + Bi_2O_3 and Al + O_2, two debris particle diameters (i.e., 0.05 and 0.1 mm), and two particle velocities indicated in the left corner of each image [(a)–(d)]. The still frames were captured from the particle combustion and fluid dynamics model videos showing burning behavior as a function of time. Note the mass fraction concentration scale bars are all the same but included in each image set for burned particles as a function of time with red indicating a higher concentration then decreasing to blue.

visual data demonstrate that smaller particle debris (1) disperse over a broader range (i.e., axial and radial directions), (2) oxidize faster, and (3) demonstrate slower propagation in the axial direction compared to larger particles.

The physical features depicted in Fig. 5 are consistent with various aspects of the experimental observations in Fig. 3. For high impact velocity and intact projectiles, flame spreading appears planar in the axial direction and highly concentrated in the radial direction, more consistent with the smaller debris field in Fig. 5. However, experimental observations may be more strongly a function of rebounding effects than debris size distribution. For all other projectiles and impact velocities, flame spreading could result from a combination of debris sizes because the spread in the radial and axial directions are represented in both particle sizes modeled in Fig. 5 showing stochastic nature of the reaction front but also dispersion in the radial direction.

Published under license by AIP Publishing.

It is interesting to note that larger particles appear to propagate further along the axial direction than smaller particles for the same time sequence in Fig. 5. One reason is that the drag acceleration due to the drag force on the larger particles, as shown in Eq. (9), is smaller than that on the smaller particles, and, therefore, the drag forces acting on smaller particles may retard propagation. This result shows that spreading rate will also be a function of particle velocity (or debris rebound velocity upon impact) such that flame spreading dynamics are more complex than simply governed by the energy associated with combusting particles but also involve physics of multiphase fluid dynamics that are a function of particle size.

These results suggest that impact reactions can be tailored toward an application. For example, a projectile can be designed to direct energy conversion upon impact at a target by limiting rebounding debris with longer projectiles. This approach would focus energy locally instead of sweeping the energy through the domain. Alternatively, projectiles may be designed to more broadly distribute energy through a chamber by promoting dispersion via fragmentation prior to target impact. Kinetic energy flux may be an indicator to enable optimization of a tailored response, although more testing is needed to reveal the usefulness of this parameter. Also, the multiple reaction pathways associated with aluminum oxidation with the solid oxidizer and oxygen from the environment may provide extended burn times to enhance the burning duration.

CONCLUSION

This study examined the visual data of flame spreading behavior of brittle thermite projectiles that reacted upon impacting a steel target at velocities of 850 and 1200 m/s. Two types of projectiles were examined: the first type fragmented upon penetrating a thin break-screen at the entrance of the reaction chamber and then impacted the target plate, and the other type remained fully intact upon impacting the target place. Overall, fragmented projectiles demonstrated well dispersed debris clouds and high flame spreading rates (e.g., 255–353 m/s) at both impact velocities. Intact projectiles demonstrated different behaviors as a function of impact velocity. At lower impact velocity of 850 m/s, the debris field resembled the fragmented case with similar flame spreading rates (e.g., 217–255 m/s). At higher impact velocity, the debris cloud was highly consolidated in the radial direction such that limited rebounding and debris dispersion may have also limited oxygen availability and contributed to the lowest spreading rate (179 m/s) observed for all cases examined. From these observations, a kinetic energy flux was proposed to correlate projectile impact conditions (i.e., velocity and projectile impact area) with flame spreading behavior. A kinetic energy flux threshold may provide an indication of debris dispersion and associated flame spreading behavior, although more testing is needed to further resolve the coupling of energy and multiphase dynamics. Additionally, a particle combustion and heat transfer model enveloped into a fluid dynamics code was applied to assess the extent of reaction and flow behavior as a function of particle size. The model showed smaller particles react at shorter time scales and exhibit enough drag to inhibit their axial propagation. The model also showed a greater contribution of aluminum oxidation from gas phase oxygen in the environment at higher particle entrained velocities because more oxygen is available to induce particle reactivity. Overall, the experiments and modeling show that flame spreading is a complex function of rebounding debris that reacts and spreads as a function of dispersion and size.

ACKNOWLEDGMENTS

The authors are grateful for support from the U.S. Air Force Research Laboratory, and M.L.P. is also thankful for partial support from the Office of Naval Research (ONR).

DATA AVAILABILITY

The data that support the findings of this study are available from the corresponding author upon reasonable request.

REFERENCES

[1] National Research Council, *Advanced Energetic Materials* (National Academic Press, 2004), Vol. 32.
[2] R. G. Ames, "Energy release characteristics of impact-initiated energetic materials," in *The Materials Research Society (MRS) Fall Meeting: Symposium H—Multifunctional Energetic Materials, Boston, USA* (MRS Online Proceeding Library Archive 896, 2005).
[3] J. P. Hooper, "Impact fragmentation of aluminum reactive materials," J. Appl. Phys. **112**, 043508 (2012).
[4] R. G. Ames, "Vented chamber calorimetry for impact-initiated energetic materials," in *The American Institute of Aeronautics and Astronautics (AIAA) Proceedings* (AIAA, 2005), p. 279.
[5] X. F. Zhang, A. S. Shi, L. Qiao, J. Zhang, Y. G. Zhang, and Z. W. Guan, "Experimental study on impact-initiated characters of multifunctional energetic structural materials," J. Appl. Phys. **113**, 083508 (2013).
[6] K. J. Hill and M. L. Pantoya, "Highly reactive pre-stressed aluminum under high velocity impact loading: Processing for improved energy conversion," Adv. Eng. Mater. **21**, 1900492 (2019).
[7] M. W. Beckstead, "Correlating aluminum burning times," Combust. Explos. Shock Waves **41**, 533–546 (2005).
[8] I. Altman, "Burn time of metal nanoparticles," Materials **12**, 1368 (2019).
[9] D. Allen, H. Krier, and N. Glumac, "Heat transfer effects in nano-aluminum combustion at high temperatures," Combust. Flame **161**, 295–302 (2014).
[10] S. Whitaker, "Forced convection heat transfer correlations for flow in pipes, past flat plates, single cylinders, single sphere, and for flow in packed beds in tube bundles," AIChE J. **18**(2), 361–372 (1972).
[11] D. J. Tritton, *Physical Fluid Dynamics*, 2nd ed. (Oxford University Press, Oxford, 1988).
[12] N. W. Piekiel, L. Zhou, K. T. Sullivan, S. Chowdhury, G. C. Egan, and M. R. Zachariah, "Initiation and reaction in Al/Bi_2O_3 nanothermites: Evidence for the predominance of condensed phase chemistry," Combust. Sci. Technol. **186**(9), 1209–1224 (2014).
[13] B. L. Werley, H. Barthelemy, R. Gates, J. W. Slusser, K. B. Wilson, and R. Zawierucha, "A critical review of flammability data for aluminum," in *Flammability and Sensitivity of Materials in Oxygen-Enriched Atmospheres Sixth Volume, ASTM STP 1197*, edited by D. D. Janoff and J. M. Stoltzfus (American Society for Testing and Materials, Philadelphia, 1993).

Published under license by AIP Publishing.